

Order-parameter coupling and strain relaxation behavior of $\text{Ti}_{50}\text{Pd}_{50-x}\text{Cr}_x$ martensites

S. L. Driver,¹ E. K. H. Salje,¹ C. J. Howard,² G. I. Lampronti,¹ X. Ding,³ and M. A. Carpenter¹ 
¹*Department of Earth Sciences, University of Cambridge, Downing Street, Cambridge CB2 3EQ, United Kingdom*
²*School of Engineering, University of Newcastle, Callaghan, New South Wales 2308, Australia*
³*State Key Laboratory for Mechanical Behavior of Materials, Xi'an Jiaotong University, Xi'an 710049, China*



(Received 6 April 2020; revised 15 June 2020; accepted 18 June 2020; published 16 July 2020)

A group theoretical model is proposed for linear/quadratic coupling between order parameters which arise from electronic and soft-mode instabilities in doped shape memory alloys, together with coupling to symmetry breaking shear strains. This model is tested by using resonant ultrasound spectroscopy (RUS) to follow the elastic and anelastic anomalies which accompany transitions from B2 to B19, 9R, and incommensurate structures in $\text{Ti}_{50}\text{Pd}_{50-x}\text{Cr}_x$ alloy samples ($0 \leq x \leq 12$). The pure soft-mode transition gives rise to an incommensurate structure but without any associated changes in the shear modulus, implying that coupling with shear strains is weak. By way of contrast, the observed pattern of softening ahead of and stiffening below the martensitic transition is typical of pseudoproper ferroelastic behavior and confirms that there is strong bilinear coupling of the tetragonal shear strain to the order parameter associated with irrep Γ_3^+ of the parent space group. The second order parameter has the symmetry properties of M_5^- in TiPd or of a point along the Σ line of the Brillouin zone for the 9R and incommensurate structures with high Cr contents. Comparison of shear modulus data for Cr-rich samples obtained by RUS at $10^5 - 10^6$ Hz with previously reported Young's modulus data obtained for different samples by dynamical mechanical analysis at $\sim 0.1-10$ Hz has not revealed the dispersion with frequency that would be expected for a glass transition governed by Vogel-Fulcher dynamics. The two techniques differ in the magnitude of effective applied stress, however, and differences in chemical homogeneity between samples or decomposition during high-temperature measurements might also be a factor.

DOI: [10.1103/PhysRevB.102.014105](https://doi.org/10.1103/PhysRevB.102.014105)

I. INTRODUCTION

Shape memory alloys have attracted intense interest for their combination of good mechanical properties and strong damping capabilities, which typically arise from a reversible martensitic transformation between a high-temperature, highly symmetric parent (austenite) phase, and a low-temperature, lower-symmetry martensite phase. Large damping is associated both with the transition itself and with the development of ferroelastic twins in the martensite phase. The most common alloy in this context is $\text{Ti}_{50}\text{Ni}_{50}$, in which the starting temperature of the martensitic transformation, M_s , is ~ 340 K. Shape memory alloys with higher M_s temperatures include those based on TiPd to which dopants have been added. At first glance the main effect of adding elements such as Cr, Fe, Co, Mn, V is simply to reduce M_s approximately linearly with composition from 810 K in the pure phase (Fig. 1). However, the more complete phase diagram shown in Fig. 2 for $\text{Ti}_{50}\text{Pd}_{50-x}\text{Cr}_x$ reveals that these materials develop different superstructures and it has been suggested that, above some critical concentration, the influence of the dopants as defects inhibits the formation of the long-range order required for the martensite phase to form. Nanosized martensitic domains may then form locally and a strain glass might develop instead of the martensite [1–4]. The phenomenological richness of this behavior, with multiple instabilities related to different driving order parameters, forms the focus of the present study in which acoustic properties of $\text{Ti}_{50}\text{Pd}_{50-x}\text{Cr}_x$ arising from strain/order-parameter coupling and ferroelastic

microstructures have been investigated by resonant ultrasound spectroscopy (RUS).

The single most important physical property in determining overall patterns of behavior in martensitic systems is strain, which provides a common thread permeating throughout all aspects of the phase relationships shown in Figs. 1 and 2. Macroscopic strains associated with martensitic transitions are substantially larger than those typically associated with ferroelastic transitions in, say, perovskites, but it is likely that the effects of local strain heterogeneity will be broadly the same. For example, local strain effects resulting from cation/vacancy disordering in $\text{La}_{0.6}\text{Sr}_{0.1}\text{TiO}_3$ act to suppress correlation of shear strains accompanying an octahedral tilting transition, but not the tilting transition itself [28]. In relaxor ferroelectrics such as $\text{Pb}(\text{Mg}_{1/3}\text{Nb}_{2/3})\text{O}_3$, a discrete ferroelectric transition is replaced by a freezing process of locally ordered domains which follows Vogel-Fulcher dynamics characteristic of a glass transition [29–32]. Addition of Cr to TiPd appears to result in both a reduction in the magnitude of macroscopic strains accompanying the transitions and a tendency towards glassy behavior.

An effective way of investigating aspects of both macroscopic and local strain is through the influence they have on elastic and anelastic properties. Dynamical mechanical analysis (DMA) has already been used to reveal diverse damping behavior of polycrystalline samples from the $\text{Ti}_{50}\text{Pd}_{50-x}\text{Cr}_x$ system [1–4,24,33]. This includes effects relating to the martensitic transition, the presence of hydrogen, and the development of a proposed strain glass. There is no single

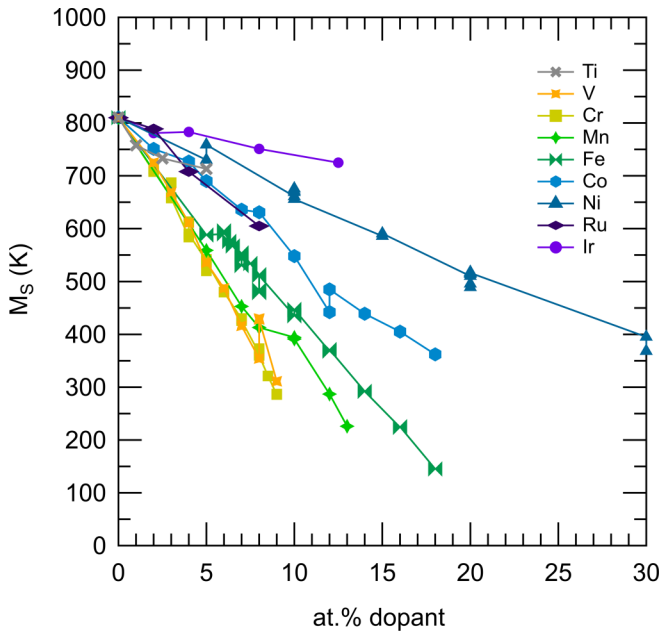


FIG. 1. Variations of M_S for $\text{Ti}_{50}\text{Pd}_{50-x}\text{X}_x$ alloys where x is the atomic % of dopant X : Ti, Ref. [5]; V, Refs. [5,6]; Cr, Refs. [6–9]; Mn, Refs. [1,7]; Fe, Refs. [1,6,7,10,11]; Co, Refs. [6,7,12]; Ni, Refs. [13–20]; Ru, Ir, Ref. [12]. Data point for Pd is average of values from Refs. [1,5,6,13,14,21–23].

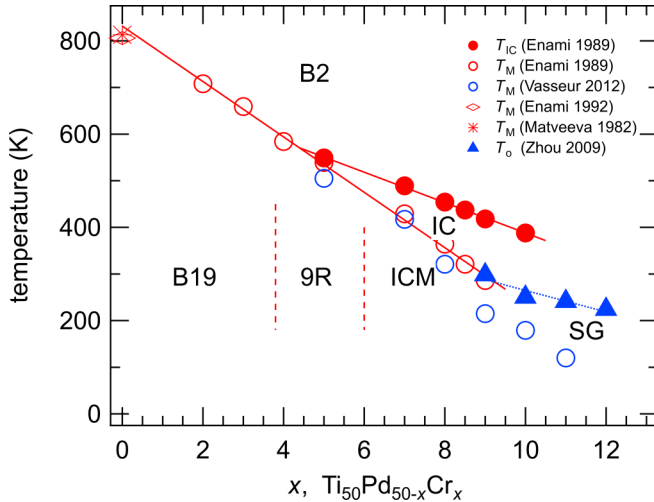


FIG. 2. Simplified phase diagram for the $\text{Ti}_{50}\text{Pd}_{50-x}\text{Cr}_x$ system showing the transition temperatures of B2-B19, B2-incommensurate (IC), IC-9R and IC-incommensurate martensite (ICM) transitions, but without showing two-phase fields. The 9R and ICM fields may have coexisting B19 [6]. T_0 is the Vogel-Fulcher temperature given by Zhou *et al.* [24] as marking the zero-frequency freezing point for the development of a strain glass. Vertical dashed lines mark approximate composition limits for different martensitic phases observed at room temperature [8,25]. Data points from: Enami *et al.* [8], Enami and Nakagawa [6], Matveeva *et al.* [26], Vasseur *et al.* [4], Shapiro *et al.* [27]). Decomposition of the B2 phase during high-temperature aging to form a precipitate with composition $\text{Ti}_{50}\text{Pd}_{25}\text{Cr}_{25}$ based on the open B2 structure has also been reported for alloys with between 8% and 15% Cr [25].

experimental method available to follow strain relaxation behavior over a wide range of time scales, however. Combinations of techniques are needed to distinguish different mechanisms such as are involved, for example, in the mobility of ferroelastic twin walls [34,35]. RUS provides information on relaxation behavior on time scales of $\sim 10^{-5} - 10^{-6}$ s, in comparison with $\sim 10^1 - 10^{-1}$ s from DMA. There is also a contrast in the magnitudes of induced strains involved in the two experimental methods which are estimated to be in the vicinity of 10^{-7} for RUS and generally $10^{-3} - 10^{-5}$ for DMA [36].

The primary objectives of the present study were to identify the combinations of order parameters needed to produce the different phase transitions observed in doped TiPd alloys, to characterize the strength of intrinsic strain/order-parameter coupling effects, and to follow the dynamical response of ferroelastic microstructures under conditions of low applied stress. A formal model of order parameter and strain coupling, based on symmetry, is given in Sec. II, and an analysis of the spontaneous strains is given in the Appendix. A secondary objective was to use the contrasting frequency ranges of RUS and DMA techniques to test for dispersion in the relaxation behavior associated with the formation of a strain glass and with the mobility of interstitial hydrogen.

II. STRUCTURAL RELATIONSHIPS, STRAIN COUPLING, AND MICROSTRUCTURE

A. Structure types and symmetry relationships

The phase diagram for the Pd-rich end of the $\text{Ti}_{50}\text{Pd}_{50-x}\text{Cr}_x$ solid solution (Fig. 2) shows the first-order martensitic transition in stoichiometric TiPd occurring at $T_M \approx 810$ K [6,26] and decreasing in temperature with increasing Cr content. The stability field of an incommensurate structure (IC) appears ahead of T_M when x is greater than ~ 4.5 , with the temperature of the transition from the parent B2 structure decreasing linearly with increasing Cr content. The low-temperature structure of stoichiometric TiPd is B19 but this gives way first to the 9R structure and then to an incommensurate martensite (ICM). Here the labels IC and ICM have been used to distinguish between the incommensurate structure above the martensitic transition (IC) from the incommensurate structure below the transition (ICM). Approximate boundaries between the low-temperature structures are shown as dashed vertical lines though, in reality, phase coexistence has been observed at several compositions. The ICM phase may be replaced by a strain glass at high Cr contents, and the reported Vogel-Fulcher freezing temperature (T_0) reduces with increasing Cr content [1–4]. Evidence from synchrotron x-ray powder diffraction is that $\text{Ti}_{50}\text{Pd}_{38}\text{Cr}_{12}$ remains cubic down to at least 125 K, while peak splitting indicative of symmetry breaking occurs between ~ 300 and ~ 250 K in $\text{Ti}_{50}\text{Pd}_{40}\text{Cr}_{10}$ [4]. The latter temperature is ~ 70 K above the value of T_M shown for this composition in Fig. 2(b) of Vasseur *et al.* [4].

The B2 structure is cubic, with space group $Pm\bar{3}m$ and reference lattice parameter a_0 . B19 (also labeled 2H or 2O in the literature [37]) is an orthorhombic structure with space group $Pmma$ and unit-cell parameters $a \approx \sqrt{2}a_0$, $b \approx a_0$, $c \approx \sqrt{2}a_0$. Doping gives rise to the 9R structure (also labeled

6M in the literature [37]), which is generally considered to be monoclinic, with space group $P2/m$. The repeat along one of the $[110]^*$ directions of the parent cubic structure contains nine planes of atoms, which corresponds to $\sim 4.5 \times \sqrt{2}a_0$. The IC structure appears to be an incommensurate version of the 9R structure with the repeat varying between 3 and 4.5 planes of atoms ($\sim 1.5 \times \sqrt{2}a_0 - \sim 2.25 \times \sqrt{2}a_0$) at $x \approx 6$ and $x \approx 14$, respectively [25,27]. Schwartz *et al.* [25] showed a systematic variation of the incommensurate repeat in $\text{Ti}_{50}\text{Pd}_{50-x}\text{Cr}_x$ with composition at room temperature but Shapiro *et al.* [27] reported a constant value of ~ 4.5 at $x = 6.5, 8.5, 10$. They also found that this was independent of temperature for samples with $x = 6.5$ and 10 .

These structures and the relationships between them can be understood in terms of different combinations of separate order parameters, as derived using the group theory program ISOTROPY [38] and set out in Table I, following Carpenter and Howard [39]. The relevant order parameters have the symmetry of an irreducible representation (irrep) belonging to the Γ point of the $Pm\bar{3}m$ Brillouin zone, Γ_3^+ , an M-point irrep, M_5^- , and irreps for the Σ line between the Γ - and M-points, i.e., along $[110]^*$ of the parent cubic structure. Transitions due to M_5^- can be Landau continuous, but transitions due to Γ_3^+ cannot. Key combinations involve the Γ_3^+ and Σ_2 irreps, which may be understood in terms of driving an electronic transition and soft-mode transition, respectively. On its own, the Γ_3^+ order parameter would lead to a tetragonal structure, $P4/mmm$, or an orthorhombic structure, $Pmmm$, depending on whether it has one $(a,0)$ or two (a,b) nonzero components. The Σ_2 order parameter has 12 components and could lead to many different subgroups of $Pm\bar{3}m$. One of the simplest has a single nonzero component and the active k vector at $1/3$ along each of the $[110]^*$ directions. This gives the R phase which competes with the martensitic phase in NiTi alloys (e.g., Ref. [40]). It has a trigonal structure and, for the order-parameter components here, would have space group $P\bar{3}$. Following Barsch [41], the transition to $Pmma$ (B19) could be driven by the M_5^- order parameter with one nonzero component alone, but with Γ_3^+ and Γ_5^+ as secondaries. If the electronic instability is important, the Γ_3^+ order parameter would also be acting as a driving order parameter, however. The B19' structure of NiTi ($P2_1/m$) requires an additional instability with Γ_5^+ as the driving order parameter. The structure corresponding to 9R in space group $P2/m$ would have Σ_2 , $\mathbf{k}_{\text{active}} = (1/9, 1/9, 0)$.

Incommensurate structures with different repeat distances would be described by irreps along the Σ line. One approach is to treat selected phases at $\mathbf{k} = (1/3, 1/3, 0)$, $(1/4, 1/4, 0)$, or $(1/5, 1/5, 0)$ as commensurate examples of the orthorhombic and monoclinic phases. In each case there are two possibilities. For $(1/n, 1/n, 0)$ with $n = \text{odd}$, the resulting structures could be orthorhombic ($Amm2$) or monoclinic ($P2/m$), depending on which components of the Γ_3^+ order parameter are nonzero. If the transition is driven by the Σ_2 order parameter alone, say as a pure soft-mode transition, $\Gamma_3^+(a,0)$ would just be a secondary order parameter and the resulting structure would have space group $Amm2$. Observation of the $P2/m$ structure, however, would be indicative that the $\Gamma_3^+(a,b)$ order parameter is also driving the transition. For $n = \text{even}$, the same argument applies and the two structures

have space groups $Pmma$ and $P2/m$, depending on whether the Γ_3^+ contribution would give rise to a tetragonal structure $(a,0)$ or an orthorhombic structure (a,b) if acting alone. In the case of $\text{Ti}_{50}\text{Pd}_{50-x}\text{Cr}_x$, the neutron-scattering study of Shapiro *et al.* [27] showed a ridge of elastic scattering along the $[110]^*$ direction of the reciprocal lattice, i.e., along the Σ line between the Γ - and M-points, implying incipient instabilities at any point along it. The observed instability was at $q = 0.22$, between $\mathbf{k} = (1/4, 1/4, 0)$ and $(1/5, 1/5, 0)$, for $x = 6.5, 8.5$, and 10 . A more rigorous treatment would be to consider all structures with Σ_2 order parameters as being incommensurate, as set out in Carpenter and Howard [39], but this is beyond the scope of what is needed for the present study.

B. Strain and order parameter coupling

Phase transitions from the parent cubic phase to any of the subgroup structures listed in Table I will be ferroelastic in character. If the driving order parameter belongs to the M-point or to the Σ line, the transitions will be improper ferroelastic but if Γ_3^+ or Γ_5^+ is also driving, it will have some significant pseudoproper component. This has implications for the form of coupling of the order parameters with strain and, hence, the forms of softening of the elastic constants, as set out in Carpenter and Salje [42]. Taking the example of the B19 structure, a Landau expansion which includes both of the Γ_3^+ and M_5^- order parameters is

$$\begin{aligned}
 G = & \frac{1}{2}a_{\Gamma}(T - T_{c\Gamma})q_{\Gamma}^2 + \frac{1}{3}b_{\Gamma}q_{\Gamma}^3 + \frac{1}{4}c_{\Gamma}q_{\Gamma}^4 \\
 & + \frac{1}{2}a_{\text{M}}(T - T_{c\text{M}})q_{\text{M}}^2 + \frac{1}{4}b_{\text{M}}q_{\text{M}}^4 \\
 & + \lambda_{a\Gamma}e_a q_{\Gamma}^2 + \lambda_{t\Gamma}e_t q_{\Gamma} + \lambda_{5\Gamma}(2e_6^2 - e_2^2 - e_5^2)q_{\Gamma} \\
 & + \lambda_{a\text{M}}e_a q_{\text{M}}^2 + \lambda_{t\text{M}}(e_t + \sqrt{3}e_o)q_{\text{M}}^2 + \lambda_{5\text{M}}e_5 q_{\text{M}}^2 \\
 & + \lambda_{6\text{M}}(e_4^2 + e_6^2)q_{\text{M}}^2 + \lambda_{q\Gamma}q_{\text{M}}^2 \\
 & + \frac{1}{6}(C_{11}^0 + 2C_{12}^0)e_a^2 + \frac{1}{4}(C_{11}^0 - C_{12}^0)(e_t^2 + e_o^2) \\
 & + \frac{1}{2}C_{44}^0(e_2^2 - e_5^2 - e_6^2). \tag{1}
 \end{aligned}$$

Here G is the excess free energy, q_{Γ} and q_{M} are components of the Γ - and M-point order parameters, a, b, c are standard Landau coefficients, λ 's are coupling coefficients, $T_{c\Gamma}$ and $T_{c\text{M}}$ are critical temperatures, e_a is the volume strain, e_t is the tetragonal shear strain, e_4, e_5, e_6 are shear strains, and $C_{11}^0, C_{12}^0, C_{44}^0$ are elastic constants of the parent cubic structure. The key features are strong coupling with shear strains characteristic of martensitic transitions, bilinear coupling between the Γ -point order parameter and the tetragonal shear strain, and linear-quadratic coupling between the two order parameters. If the transition is driven exclusively by the M-point order parameter, the elastic constants should display the pattern of improper ferroelastic behavior, with more or less constant values above the transition point and the transition itself marked by abrupt (discontinuous) softening. If the Γ -point order parameter is driving, a pseudoproper pattern should be observed, with the elastic constant combination $C_{11} - C_{12}$ showing steep softening with falling temperature towards the transition point.

The phase diagram (Fig. 2) shows that there are at least two separate discrete instabilities in the $\text{Ti}_{50}\text{Pd}_{50-x}\text{Cr}_x$ system.

TABLE I. Symmetry relationships, order parameters, and unit-cell configurations for selected subgroups of space group $Pm\bar{3}m$, as derived using the group theory program ISOTROPY [38], following Carpenter and Howard [39]. Labels in the last column are taken from the literature, including, in particular, Otsuka *et al.* [37].

	Γ_3^+	Γ_5^+	M_5^-	Σ_2	$\mathbf{k}_{\text{active}}$	Basis vector	Origin	Approximate unit cell in relation to the parent cubic cell	Other labels
$Pm\bar{3}m$	(0,0)				(0,0,0)	(1,0,0),(0,1,0),(0,0,1)	(0,0,0)	a_0	B2
$P4/mmm$	(a,0)				(0,0,0)	(1,0,0),(0,1,0),(0,0,1)	(0,0,0)	a_0, a_0, a_0	L1o
$Pnmm$	(a, b)				(0,0,0)	(1,1,0),(-1,1,0),(0,0,1)	(0,0,0)	a_0, a_0, a_0	
$Cnmm$	(a,0)	(b,0,0)			(0,0,0)	(1,1,0),(-1,1,0),(0,0,1)	(0,0,0)	$\sqrt{2}a_0, \sqrt{2}a_0, a_0$	
$Pmma$	(a, $-\sqrt{3}a$)	(0,0,b)	(0,0,c, c,0,0)		(1/2,0,1/2)	(1,0,-1),(0,1,0),(1,0,1)	(1/2,0,0)	$\sqrt{2}a_0, a_0, \sqrt{2}a_0$	B19, 2H or 2O
$P2/m$	(a, b)	(0,0,c)	(0,0,d, e,0,0)		(1/2,0,1/2)	(1,0,-1),(0,1,0),(1,0,1)	(1/2,0,0)	$\sqrt{2}a_0, a_0, \sqrt{2}a_0$	
$P2_1/m$	(a, $-\sqrt{3}a$)	(b, b, c)	(0,0,d, d,0,0)		(0,0,0), (1/2,0,1/2)	(0,1,0),(-1,0,1),(1,0,1)	(0,0,1/2)	$a_0, \sqrt{2}a_0, \sqrt{2}a_0$	B19 ^c
$P\bar{3}$	(0,0)	(a, -a, a)		(b,0,0,0,0,0,0,0,0,0,0,0)	(1/3,1/3,0), (1/3,0,1/3), (0,1/3,-1/3)	(1,-1,2),(1,2,-1),(-1,1,1)	(0,0,0)	rhombohedral cell: $3a_0$, $3a_0, 3a_0$	R phase ^b
$Amn2$	(a,0)	(b,0,0)		(0,c,0,0,0,0,0,0,0,0,0,0)	(1/3,1/3,0)	(0,0,1),(3,3,0),(-1,1,0)	(0,0,0)	$a_0, 3\sqrt{2}a_0, \sqrt{2}a_0$	
$P2/m$	(a, b)	(c,0,0)		(d,0,0,0,0,0,0,0,0,0,0,0)	(1/3,1/3,0)	(-1,1,0),(0,0,1),(2,1,0)	(0,0,0)	monoclinic cell: $\sqrt{2}a_0, a_0, \sqrt{5}a_0$	3R or 2M ^a
								$\beta \approx [90 + \tan^{-1}(1/3)]^\circ = 108^\circ$	
$Pmma$	(a,0)	(b,0,0)		(c,0,0,0,0,0,0,0,0,0,0,0)	(1/4,1/4,0)	(2,2,0),(0,0,1),(1,-1,0)	(0,0,0)	$2\sqrt{2}a_0, a_0, \sqrt{2}a_0$	
$P2/m$	(a,b)	(c,0,0)		(d,0,0,0,0,0,0,0,0,0,0,0)	(0,0,0) (1/4,1/4,0)	(-1,1,0),(0,0,1),(2,2,0)	(0,0,0)	$\sqrt{2}a_0, a_0, 2\sqrt{2}a_0$	
$Amn2$	(a,0)	(b,0,0)		(0,c,0,0,0,0,0,0,0,0,0,0)	(1/5,1/5,0)	(0,0,1),(5,5,0),(-1,1,0)	(0,0,0)	$a_0, 5\sqrt{2}a_0, \sqrt{2}a_0$	
$P2/m$	(a, b)	(c,0,0)		(d,0,0,0,0,0,0,0,0,0,0,0)	(1/5,1/5,0)	(-1,1,0),(0,0,1),(3,2,0)	(0,0,0)	monoclinic cell: $\sqrt{2}a_0, a_0, \sqrt{13}a_0$	5M or 10M
								$\beta \approx [90 + \tan^{-1}(1/5)]^\circ = 101^\circ$	

^aNote that “other labels” for the $P2/m$ structure with $\mathbf{k}_{\text{active}} = (1/2, 0, 1/2)$ were incorrectly given as “3R or 2M” in Table III of Ref. [39]. These are shown correctly here as being other labels for the $P2/m$ structure with $\mathbf{k}_{\text{active}} = (1/3, 1/3, 0)$. Similarly Table III of Ref. [39] has “9R or 6M” as other labels for the $P2/m$ structure with $\mathbf{k}_{\text{active}} = (1/3, 1/3, 0)$, whereas these are really other labels for the $P2/m$ structure with $\mathbf{k}_{\text{active}} = (1/9, 1/9, 0)$

^bA rhombohedral setting for the unit cell of the R phase is included, as in Ref. [39], though here with a smaller unit cell.

The IC structure appearing by a second-order transition at T_{IC} is driven exclusively by a Σ_2 order parameter, with little or no strain coupling. It can then be argued that this couples with the Γ -point order parameter to generate the B19, 9R, and ICM structures. The coupling is linear quadratic in form, which gives rise to particular sequences of transitions, depending on the strength of the coupling and the relative critical temperatures. Salje and Carpenter [43] showed that, in the simple case of linear-quadratic coupling, λQP^2 , for two instabilities with critical temperatures, T_{cQ} , T_{cP} , the circumstance $T_{cQ} < T_{cP}$ gives rise to a single transition because the order parameter P acts as a field for the order parameter Q . Alternatively, for $T_{cQ} > T_{cP}$, the sequence can be a second-order transition to a structure with $Q \neq 0$, $P = 0$, followed by a first-order transition to a phase with $Q \neq 0$, $P \neq 0$. In $\text{Ti}_{50}\text{Pd}_{50-x}\text{Cr}_x$, Q would correspond to q_Γ and P to an incommensurate order parameter, q_{IC} , with a crossover between two sequences, B2-B19, B2-B19-ICM, at $x \sim 4.5$.

The observed sequence B2($P = 0$, $Q = 0$) – IC($P \neq 0$, $Q = 0$) – ICM($P \neq 0$, $Q \neq 0$) does not fit with what is predicted from the generalized treatment, implying that q_{IC} does not have significant linear/quadratic coupling with the Γ_3^+ order parameter. This would be possible if the order parameter did not couple with shear strain, and it is important to observe whether it is the case. On the other hand, the 9R and ICM phases appear at a discrete first-order transition, implying strong coupling between Γ_3^+ and Σ_2 order parameters in these structures, most likely through their coupling to common strains. A dominant role for the Γ -point order parameter will be identifiable as pseudoproper elastic softening ahead of the martensitic transitions.

C. Microstructures

The dominant microstructure of the martensitic phases involves ferroelastic twin walls, as observed on a scale of ~ 100 – 200 nm by transmission electron microscopy (TEM) [8,25,44,45]. Also expected are antiphase domains arising from the decreases in translational symmetry. These have been observed on a scale of ~ 50 nm in a dark field TEM image from $\text{Ti}_{50}\text{Pd}_{41}\text{Cr}_9$ by Enami *et al.* [8] and of several tens of nm in a sample with the same nominal composition by Zhou *et al.* [3]. High-resolution TEM images reveal the periodicity of incommensurate domains to be on a scale of ~ 0.6 – 1 nm [25,44,45]. Finally, a tweed microstructure has been reported as the characteristic precursor to martensitic transitions [4,27]. A suggestion based on diffuse intensity in neutron-diffraction patterns has been that this starts to develop at temperatures perhaps as high as ~ 1200 K, with a temperature dependence that is distinctly different from that of the IC structure [27].

III. EXPERIMENTAL METHODS AND SAMPLE CHARACTERIZATION

$\text{Ti}_{50}\text{Pd}_{50-x}\text{Cr}_x$ ingots with $x = 0, 4, 5, 6, 7, 8, 9, 10, 11, 12$ at. % (abbreviated in the following as 0Cr, 4Cr, etc.) were prepared by arc melting of Ti, Pd, and Cr with 99.9% purity under argon atmosphere. The ingot was annealed at 900°C , and hot rolled to a thin plate with thickness 1.5 mm. The possible oxidation layer at the surface was removed by mechanical

polishing with sandpaper. Samples for RUS testing were cut from the plate into the shape of a rectangular parallelepiped with dimensions of approximately $1 \times 2 \times 3 \text{ mm}^3$. It should be noted that the samples used for previous DMA and TEM studies were cut from different ingots which had been prepared by induction melting, followed by casting into a copper mold with cylindrical shape [1–4,24].

Separate instruments used for the high- and low-temperature RUS measurements have been described by McKnight *et al.* [46,47], and general principles of the method have been set out elsewhere [48]. In measurements above room temperature, the sample was held between two alumina rods and inserted horizontally into a Netzsch 1600°C furnace. The driving and receiving transducers were attached to the ends of the rods, outside the furnace. Argon gas flowed through the furnace during the experiment to minimize oxidation of the samples. Resonance spectra were collected in the frequency range 100–600 kHz during automated heating and cooling runs, with 40 000 data points collected in each spectrum. A settle time of 120 s at each temperature was used to allow thermal equilibration before data were collected, and the overall rate of data collections was ~ 1 spectrum per hour. The surface of each sample was discolored after heating, suggesting that some slight surface oxidation had occurred.

Following high-temperature measurements, the samples were transferred to the low-temperature apparatus, in which they sat directly between the two transducers in a helium flow cryostat. Spectra containing 65 000 data points were collected in the frequency range 100–1200 kHz after a 20-min thermal equilibration period at each temperature. Details of the full sequences of data collection for each sample are given in Table II.

Selected resonance peaks were fitted with an asymmetric Lorentzian function within the software package IGOR (Wave-metrics), allowing peak frequency f and the full width at half of the maximum height Δf to be followed as a function of temperature. The elastic moduli scale with f^2 and acoustic loss can be represented in terms of the inverse mechanical quality factor, Q^{-1} , which was taken as $Q^{-1} = \Delta f/f$. Natural resonances of a small object are determined predominantly by shearing motions with, in general, only small contributions from breathing motions. As a result, the temperature dependence of f^2 from individual resonance peaks in spectra collected from a polycrystalline sample provide a good representation of the temperature dependence of the shear modulus.

X-ray-diffraction patterns from lab-based equipment have been reported in the literature for compositions between 4Cr and 5Cr [33], 5Cr [2], 9Cr [3], and 10Cr [24]. 4Cr was shown to possess the B19 structure at room temperature, as expected [33]. 5Cr was shown to have the B2 structure at 563 K and the B19 structure at 298 K [2]. 9Cr showed no evidence of distortion from cubic lattice geometry at 160, 293, or 373 K [3], while 10Cr remained metrically cubic at 223, 293, and 373 K [24]. In diffraction patterns with higher resolution from synchrotron measurements on a different sample of 10Cr, distinct peak splitting occurred at 252 K down to at least 125 K and the responsible structure type was determined as 9R [4]. Changes in spacing of diffraction peaks from these data (reproduced below in the Appendix) show that, although they converge slightly with increasing temperature, there is still a

TABLE II. Details of the heating and cooling cycles for each of the samples. Temperatures quoted here are for set points of the control thermocouple in the windings of the furnace for the automated sequences; actual temperatures were recorded by a thermocouple placed within a few mm of the sample.

Sample	Experimental details
0Cr	HT: 303–843 K in 10-K steps; 846–1005 K in 3-K steps (and reverse) LT: 280–10 K in 30-K steps; 10–305 K in 5-K steps
4Cr	HT: 313–593 K in 30-K steps; 596–793 K in 3-K steps (and reverse) LT: 280–10 K in 30-K steps; 10–305 K in 5-K steps
5Cr	HT: 303–583 K in 10-K steps; 585–753 K in 3-K steps; 763–773 in 10-K steps (and reverse) LT: 280–10 K in 30-K steps; 10–305 K in 5-K steps
6Cr	HT: 300–555 K in 10-K steps; 558–720 K in 3-K steps; 730–750 K in 10-K steps LT: 295–10 K in 30-K steps; 10–305 K in 5-K steps
7Cr	HT: 293–823 K in 5-K steps (and reverse) LT: 295–10 K in 30-K steps; 10–305 K in 5-K steps
8Cr	HT: 300–340 K in 10-K steps; 343–667 K in 3-K steps; 670–720 K in 10-K steps (and reverse) LT: 280–10 K in 30-K steps; 10–305 K in 5-K steps
9Cr	HT: 293–773 K in 3-K steps (and reverse) LT: 280–10 K in 30-K steps; 5–255 K in 5-K steps; 255–305K in 1-K steps
10Cr	HT1: 300–690 K in 3-K steps; 700–740 K in 10-K steps (and reverse) LT: 280–10 K in 30-K steps; 10–160 K in 5-K steps; 162–290 K in 2-K steps HT2: 295–840 K in 5-K steps (and reverse)
11Cr	HT: 303–593 K in 10-K steps; 596–773 K in 3-K steps; 783–873 K in 10-K steps (and reverse) LT: 280–10 K in 30-K steps; 10–95 K in 5-K steps; 95–125 K in 1-K steps; 125–225 K in 5-K steps; 225–260 K in 1-K steps; 260–305 K in 5-K steps
12Cr	HT1: 293–593 K in 10-K steps; 596–773 K in 3-K steps; 783–873 K in 10-K steps (and reverse) LT1: 280–10 K in 30-K steps; 10–215 K in 5-K steps; 215–255 K in 1-K steps; 255–305 K in 5-K steps HT2: 295–880 K in 5-K steps (and reverse) LT2: 280–10 K in 30-K steps; 10–220 K in 5-K steps; 220–250 K in 1-K steps; 250–305 K in 5-K steps

substantial discontinuity at the transition temperature of ~ 300 K. This implies that the martensitic transition is first order in character at all compositions between 0 and at least 10% Cr. The same splitting was not seen in diffraction patterns from 12Cr, which was assumed to remain metrically cubic down to at least 125 K [4].

Segments of diffraction patterns collected in Cambridge from the RUS samples, before and after the complete sequence of high- and low-temperature measurements, are shown in Fig. 3. Below these are segments of patterns in the same 2θ range, reproduced from Fig. 1 of Zhou *et al.* [2] for 5Cr in the B2 and B19 phases. The starting states of samples with low Cr contents had patterns similar to the reference diffraction pattern for the B19 structure, consistent with the phase diagram shown in Fig. 2. However, samples with 9% Cr and above gave diffraction patterns, both before and after the RUS experiments, which do not match with that of the B2 structure. The final states of the low Cr samples gave patterns less obviously similar to the B19 pattern, with 4Cr giving many additional peaks. It is known that a secondary phase may form at elevated temperatures in alloys containing between 8% and 15% Cr [45]. The samples were not completely homogeneous before heating and it is possible that a secondary phase may have formed during the course of RUS data collection at high temperatures.

IV. RUS RESULTS

The evolution of f^2 with temperature for all the $\text{Ti}_{50}\text{Pd}_{50-x}\text{Cr}_x$ samples is shown in Fig. 4. In each case,

the legend indicates the sequence in which the experiments were conducted, with HT and LT denoting high- and low-temperature experiments, respectively, as set out in detail in Table II. Frequencies given in the captions indicate the values of f for the specific resonance at room temperature, with “sc” indicating where the values were scaled to the value of another resonance at room temperature for comparative purposes. Individual resonance peaks were too broad or noisy to allow reliable fitting in some temperature intervals, but it was still possible to follow their positions semiquantitatively. Variations of f^2 in these cases are shown as colored, dotted lines rather than discrete symbols. Vertical dotted lines mark the temperatures at which minima in f^2 occurred during the first heating, T_{mfh} , and cooling, T_{mfc} , cycle. Solid vertical lines are the expected transition temperatures for the B2-IC transition taken from Fig. 2. Also marked on the left side of each figure is the ratio of the maximum to minimum values of f^2 , as an expression of the total amount of elastic softening or stiffening.

The well defined minimum in f^2 in every data set has been taken as corresponding to the martensitic transition temperature, T_{mfh} during heating and T_{mfc} during cooling. Values of T_{mfc} decrease with increasing dopant levels up to 9Cr and then become approximately constant near 300 K. The overall pattern of variation with temperature also changes systematically as a function of composition. In the results for the 0Cr sample, f^2 decreases slightly (elastic softening) as the transition point is approached from above followed by a steep increase (elastic stiffening) at the austenite-martensite transition. Below the transition there is slight softening down

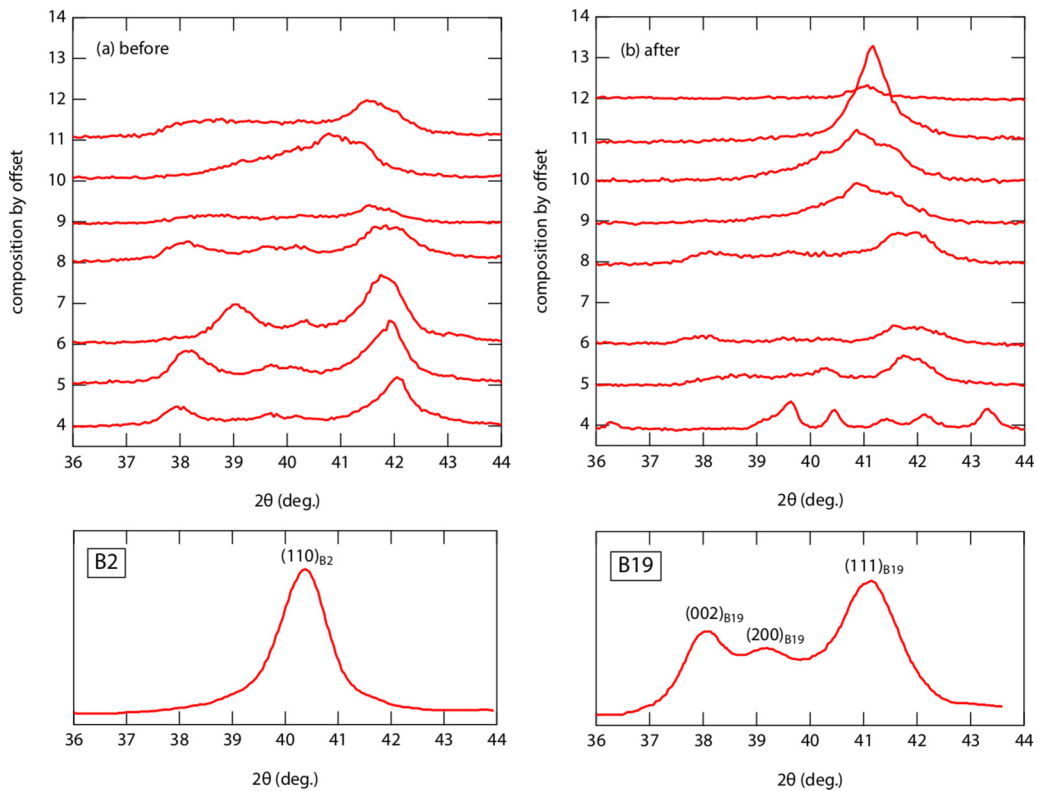


FIG. 3. Top: XRD patterns obtained using a D8-advance diffractometer with $\text{CuK}\alpha$ radiation for a subset of the samples at room temperature (a) before and (b) after completion of the RUS experiments. The diffraction geometry was Bragg-Brentano and the data were collected from one flat side of each polycrystalline sample. Note that the y axis is intensity in arbitrary units but diffraction patterns have been offset upwards in proportion to their Cr contents and the axis relabeled as values of x in $\text{Ti}_{50}\text{Pd}_{50-x}\text{Cr}_x$. Bottom: Patterns expected for samples in the B2 and B19 phase, as reproduced from Fig. 1 of Zhou *et al.* [2] for 5Cr.

to ~ 100 K, followed by a steeper trend of stiffening below ~ 100 K. The results for 4Cr are similar, though with a less steep change in f^2 at the transition point and continued stiffening at lower temperatures rather than the plateau with slight softening seen for 0Cr. The break in slope at ~ 100 K is still evident. With increasing Cr content, the patterns of softening and stiffening become more or less symmetrical about the minima in f^2 and the break in slope below ~ 100 K disappears.

The clear temperature hysteresis represented by differences between T_{mfh} and T_{mfc} is typical of martensitic alloys with first-order transition mechanisms. There is also some evidence for an additional dependence on thermal history in that the hysteresis is most marked in data from the first HT heating and cooling cycle. In cases where the high-temperature measurements were repeated (4Cr, 10Cr, 12Cr), T_{mfh} was higher in the first cycle than in the second cycle, implying that irreversible changes had occurred during the first excursion to high temperatures.

Variations of Q^{-1} , representing acoustic loss, are shown in Fig. 5 for the same resonance peaks as were used to determine the variations of f^2 . Dashed vertical lines represent T_{mfh} and T_{mfc} taken from Fig. 4. The patterns of loss fall into three groups. Data for the 0Cr sample show only minor anomalies near T_{mfh} and T_{mfc} , and the values of Q^{-1} in an interval of ~ 100 K below the transition are closely similar to their values above the transition. There is then a steep increase in

loss to the extent that the peaks became too broad to allow reliable fitting, followed by a steep decrease in a manner that resembles two sides of a Debye peak centered at ~ 400 K. Samples 4Cr to 8Cr show an increase in Q^{-1} coinciding with T_{mfh} and T_{mfc} followed by a plateau which persists down to the lowest temperatures. For samples 9Cr to 12Cr, there is an increase in Q^{-1} at T_{mfh} and T_{mfc} , followed by a peak in the loss centered around 250 K.

In both the elastic (Fig. 4) and anelastic data (Fig. 5), solid black lines indicate the expected transition temperature for the formation of the IC phase (T_{IC}) from Fig. 2. Where T_{IC} falls at temperatures that are clearly separate from the minima in f^2 (6Cr and above, but not 11Cr), there is no overt sign of any anomalies in either f^2 or Q^{-1} associated with this transition.

V. DISCUSSION

A. Strain coupling: Elastic and anelastic effects at RUS frequencies

1. $q_{\Gamma}(\Gamma_3^+)$ as the dominant order parameter

Steep elastic softening with falling temperature in the stability field of the cubic austenite structure of the samples investigated in the present study confirms the dominance of the Γ_3^+ order parameter in driving the martensitic transition at all compositions. This softening has the characteristic pattern of pseudoproper ferroelastic behavior arising from bilinear

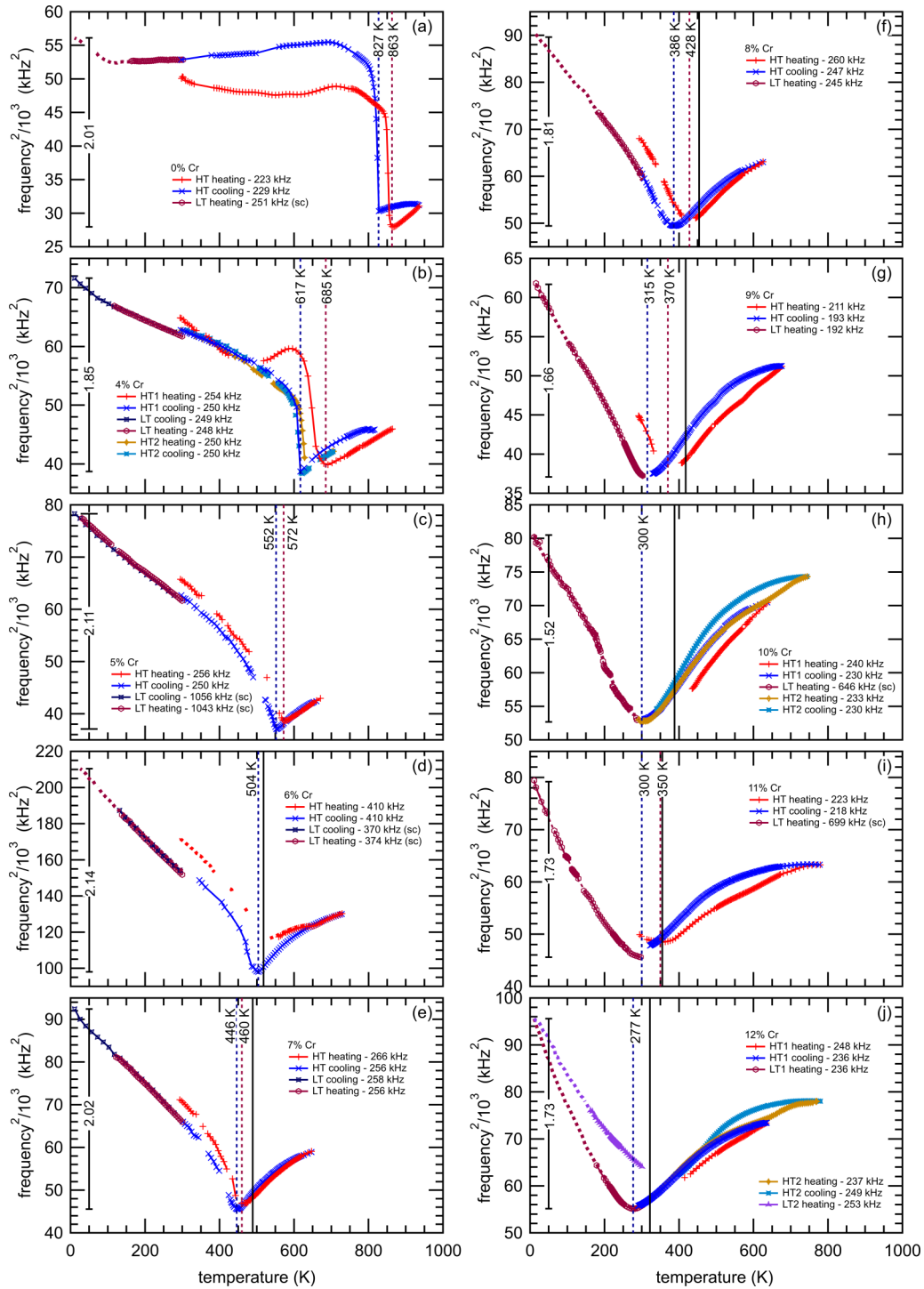


FIG. 4. Variations of f^2 with temperature for the $\text{Ti}_{50}\text{Pd}_{50-x}\text{Cr}_x$ samples. Values of f^2 from peak fitting are shown as markers, with semiquantitative data shown as dotted lines. The lists in captions indicate the sequences in which the data were collected. Vertical dashed lines indicate temperatures at which the minimum value of f^2 occurred on first heating (T_{mfh}) and cooling (T_{mfc}). The solid vertical line indicates the temperature at which the B2-IC transformation was expected to occur (T_{IC}), as taken from Fig. 2. Values of T_{IC} for 11Cr and 12Cr are extrapolations from Fig. 2. The vertical line and the number on the left side of each graph show the change in f^2 expressed as the ratio of the maximum and minimum values. For example, f^2 values for the resonance shown in (a) for the sample with 0% Cr changed by a total of a factor of 2.01. This means that the shear modulus also changes by a factor of ~ 2 between maximum and minimum values in the temperature interval ~ 10 –950 K.

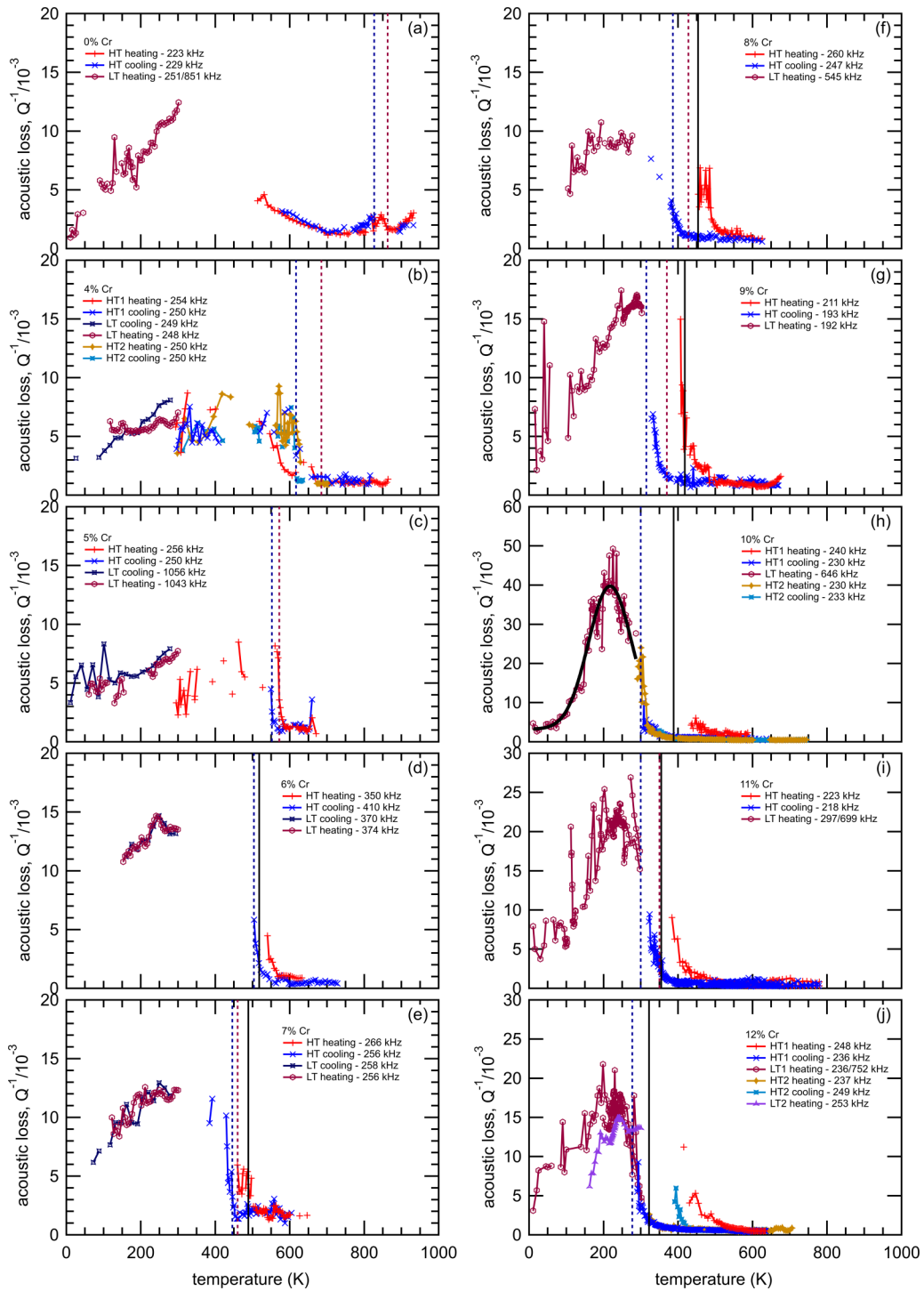


FIG. 5. Evolution of Q^{-1} with changing temperature from the resonance peaks for which values of f^2 are given in Fig. 4. Note the different scale on the y axis for 10Cr, 11Cr, and 12Cr. The caption order indicates the sequence in which the data were collected. Vertical lines indicate the temperatures T_{mfh} , T_{mfc} , and T_{IC} , as previously shown in Fig. 4. The black curve superimposed on the data for 10Cr is a fit of Eq. (2) with $E_{act}/r_2(\beta) = 6.1 \text{ kJ mole}^{-1}$.

coupling of the symmetry-adapted strain e_t with the Γ_3^+ order parameter, as specified by the term $\lambda_{t\Gamma} e_t q_\Gamma$ in Eq. (1). The Landau expansion contains third-order terms in q_Γ so that the transition is necessarily first order if its energy coefficient is finite. First-order character is, in turn, confirmed by large values of symmetry-breaking shear strains as a function of

composition at room temperature, and by the discontinuity at the transition temperature implied by the temperature dependence of peak splitting in x-ray-diffraction patterns given by Vasseur *et al.* [4] for 10Cr (see Appendix, Figs. 10 and 11). An additional driving order parameter is needed to produce each of the B19, 9R, and ICM structures, but if the M_5^- or

Σ order parameters acted alone, the elastic anomalies would be more typical of improper ferroelastics. Rather than steep precursor softening, shear elastic constants C_{11} - C_{12} and C_{44} would display slight stiffening with falling temperature due to the normal effects of thermal expansion followed by a steplike softening at the transition point due to strain coupling of the form $\lambda e q^2$, as specified by terms such as $\lambda_{1M}(e_t + \sqrt{3}e_o)q_M^2$ and $\lambda_{5M}e_5q_M^2$ in Eq. (1).

2. B2-B19: 0Cr, 4Cr

In 0Cr the B19 structure develops directly from the B2 parent structure, with q_Γ and q_M as the two order parameters [Eq. (1), Table I]. The shear modulus depends on shear elastic constants which are modified by coupling of strain with the driving order parameters. The dominant change will be from those order parameters for which coupling with the related shear strain is strongest. From the values of the symmetry breaking shear strains at room temperature, $e_{ty} \approx 19\%$ and $e_5 \approx 7\%$ (see the Appendix, Table III), it is clear that the dominant contribution will come from C_{11} - C_{12} due to $\lambda_{1\Gamma}e_tq_\Gamma$. The steep stiffening in a small temperature interval below the transition temperature (Fig. 4) is thus consistent with the strongly first-order transition and pseudoproper ferroelastic character, as shown in Fig. 5(f) of Carpenter and Salje [42]. Any softening contribution from C_{11} - C_{12} and C_{55} due to coupling of e_{ty} and e_5 with q_M^2 must be small in comparison as it is apparently not large enough to be seen overtly in the evolution of resonance frequencies of the sample. A stepwise increase in the shear modulus could come from a coupling term of the form $\lambda e_5^2q_M^2$. This would result in stiffening of C_{55} that scales with q_M^2 , but single-crystal data will be needed to distinguish in detail between the contributions of different components of the shear modulus.

A slight increase in acoustic loss in the vicinity of the transition temperature of 0Cr (Fig. 5) can be accounted for by the mobility under external stress of interfaces between cubic and martensitic phases in an interval of two-phase coexistence. By analogy with transitions in perovskites such as LaAlO_3 [49–51], it might be expected that mobile ferroelastic twin walls in the low-temperature phase would give rise to high acoustic loss and additional softening in some temperature interval immediately below the transition point. This is not observed, however, signifying that the twin walls do not move on a time scale of $\sim 10^{-5}$ to 10^{-6} s at the low stress levels of an RUS experiment. This has been explained elsewhere for the case of a CuAlBe martensite as being due to the strong pinning effect of dislocations which form part of the transformation microstructure when the spontaneous shear strains are large [52]. There is, nevertheless, an increase in Q^{-1} below ~ 700 K which becomes a broad peak marking a Debye-like acoustic loss process centered on ~ 400 K (Fig. 5). The peak is not accompanied by obvious changes in the evolution of f^2 , signifying that the loss mechanism does not give substantial changes in elastic moduli. Small displacements of some component of the ferroelastic microstructure, such as the dislocations themselves, are the likely cause, with their motion becoming progressively restricted by pinning processes below ~ 400 K.

Essentially the same pattern of elastic and anelastic anomalies is seen in the data from 4Cr, though with a smaller

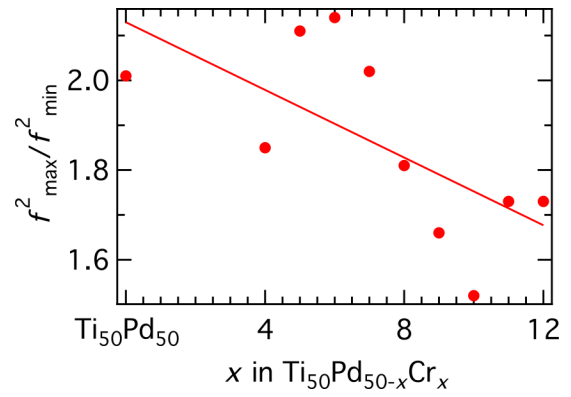


FIG. 6. Ratio of maximum to minimum values of f^2 for compositions between 0 and 12% Cr, as shown in Fig. 4. The straight line is a guide to the eye to illustrate the trend of lowering values with increasing Cr content.

increase in stiffness immediately below the transition point. Any anelastic loss which could be attributed to mobile interfaces between coexisting phases is again small but, by way of contrast from the temperature interval of ~ 200 K below the transition point in 0Cr, Q^{-1} increases immediately below the transition point. This difference may be accounted for by the reduction in transition temperature from ~ 850 to ~ 650 K which results in the transition itself encroaching onto the temperature interval within which the mobile component of the ferroelastic microstructure becomes pinned.

3. B2-IC-9R/ICM: 5Cr-12Cr

At higher Cr contents, the martensitic transition is preceded by the development of the IC structure, for which the driving order parameter has the symmetry properties of an irrep related to the Σ line between Γ - and M-points of the Brillouin zone. The expected B2-IC transition temperatures are known from the phase diagram (Fig. 2), but there are no obvious associated anomalies in the data for f^2 or Q^{-1} . It follows that the magnitudes of any strain coupling with the IC order parameter must be weak (Figs. 4 and 5). This order parameter replaces M_5^- as the second order parameter and becomes Σ_2 in the (commensurate) 9R phase (Table I). The 9R structure is expected to be monoclinic, due to the second component of the Γ_3^+ order parameter, giving a strain coupling term of the form $\lambda_{1\Gamma}(e_tq_{\Gamma t} - e_oq_{\Gamma o})$, where $q_{\Gamma t}$ and $q_{\Gamma o}$ represent the two components, rather than $\lambda_{1\Gamma}e_tq_\Gamma$ alone. There are no data available for $\text{Ti}_{50}\text{Pd}_{50-x}\text{Cr}_x$ but the additional e_o strain is ~ 3 –4% in the closely analogous $\text{Ti}_{50}\text{Pd}_{50-x}\text{Fe}_x$ system (see the Appendix, Table IV). The crossover between order parameters is accompanied by a change from the steep increase in f^2 below the transition point seen for 0Cr and 4Cr to a more continuous increase seen for 5Cr-12Cr (Fig. 4). There is also a reduction in the total effect of strain, as reflected in the decreasing ratio with increasing Cr content of the maximum observed values of f^2 to their minimum values at the martensitic transition temperature T_{mth} (Fig. 6).

4. Acoustic loss mechanisms

The pattern of acoustic loss does not change with increasing Cr content, except that continuing lowering of the transition temperature into the interval of high acoustic loss causes the pattern of Q^{-1} variations to have the appearance of a progressively narrower peak (Fig. 5). If this peak is treated in terms of a normal thermally activated pinning process, it would be expected to follow the temperature dependence given by [53,54]

$$Q^{-1}(T) = Q_m^{-1} \left[\cosh \left\{ \frac{E_{\text{act}}}{Rr_2(\beta)} \left(\frac{1}{T} - \frac{1}{T_{\text{max}}} \right) \right\} \right]^{-1}, \quad (2)$$

where Q_m^{-1} is the maximum value of Q^{-1} , occurring at temperature T_{max} , R is the gas constant, and E_{act} is the activation energy. $r_2(\beta)$ is the relative width of the acoustic loss peak assuming a Gaussian distribution of relaxation times, compared to the width of a classical Debye peak which has a single relaxation time [55]. A fit of Eq. (2) to the peak in the Q^{-1} data from 10Cr gives the values of $E_{\text{act}}/r_2(\beta)$ as ~ 6 kJ mole $^{-1}$ [Fig. 5(h)]. This is an order of magnitude smaller than values of $\sim 60 - 70$ kJ mole $^{-1}$ associated with acoustic losses due to the presence of hydrogen, but is closely similar to the value of ~ 7.5 kJ mole $^{-1}$ obtained from Vogel-Fulcher analysis of the dip in modulus of hydrogen-free Ni₅₂Ti₄₈ [56].

Although the mechanisms have not yet been identified, continuing loss processes would account for the breaks in slope of f^2 below ~ 100 K seen in the data for 0Cr and 4Cr. The elastic moduli are expected to have zero slope as temperature tends to 0 K, but this is not observed in the trends shown by f^2 in Fig. 4. It thus appears that anelastic pinning/freezing processes continue to the lowest temperatures at which measurements were made (~ 10 K).

The only evidence for a change in elastic or anelastic properties associated with the formation of a tweed microstructure ahead of the martensitic transition is a slight increase in Q^{-1} below ~ 360 K in the data for 10Cr [Fig. 5(h)]. This appears to correlate with TEM evidence of a distinct tweed microstructure in the interval $\sim 300-330$ K [4]. A similar tail in Q^{-1} is evident in data from other samples but there are no direct observations of tweed microstructures at these compositions for our samples.

B. Dispersion of elastic/anelastic properties with frequency

Dispersion with frequency in any dynamical measurements can provide insights into the mechanisms of relaxational processes such as pinning of defects or glassy freezing. In the case of RUS, the accessible resonances of mm-sized samples fall in the frequency range $\sim 10^5 - 10^6$ Hz, which is generally too narrow to resolve dispersion effects directly. However, DMA measurements on TiPdCr alloys have previously been made in the range 0.2–20 Hz, which means that softening and loss mechanisms can be compared at two widely different frequencies.

Figure 7 shows DMA data from Zhou and co-workers [2,24] and RUS results from Figs. 4 and 5 for the evolution of the elastic moduli and acoustic loss of 5Cr and 10Cr during cooling. DMA data for a 5Cr sample doped with hydrogen are shown as dashed purple lines and data for the 5Cr sample

after dehydrogenation are shown as solid green lines. The DMA sample of 10Cr was not treated in any special way for hydrogen content. f^2 values from RUS have been scaled relative to the value measured at the lowest temperature. Q^{-1} data from RUS measurements have been divided by $\sqrt{3}$ to allow comparison with $\tan\delta$ from DMA according to the relationship (for small losses) [57,58] $\tan\delta = Q^{-1}/\sqrt{3}$.

1. Absence of dispersion shown by elastic moduli

The overall patterns of softening and stiffening represented by the storage modulus from DMA and f^2 from RUS are qualitatively the same. They are both consistent with pseudoproper ferroelastic character for the first-order martensitic transition. The similarities also confirm that the overall behavior is not substantially affected by heterogeneities in the samples. All compositions quoted here and in the literature are nominal, relating to the starting composition before crystal growth. The actual compositions may differ, which would account for the differences in transition temperatures shown in Fig. 7.

Frequency dispersion for the temperature at which the minimum in storage modulus occurs in 10Cr at DMA frequencies was interpreted in terms of a glass transition, following the Vogel-Fulcher relationship, $\omega = \omega_0 \exp\left(\frac{-E_{\text{act}}}{R(T_g - T_0)}\right)$ [24]. Here ω is the angular frequency ($= 2\pi f$, where f is the measuring frequency), ω_0 is a constant, T_g is the temperature at which the storage modulus has its minimum value at a certain frequency and T_0 is the value of T_g at 0 Hz. The same conclusion was drawn from variations in T_g for other samples with compositions between 9Cr and 12Cr [3,4,24]. Reported values of T_0 obtained from fitting of the Vogel-Fulcher equation were 298 K for 9Cr [3] and 250 K for 10Cr [4,24], but values of E_{act} were not given. If the martensitic transition was governed by Vogel-Fulcher dynamics in this way, the temperatures at which minima in f^2 occur at RUS frequencies should be substantially higher than the temperatures at which the minima in storage modulus occur. As shown in Fig. 8, however, the temperatures of these minima actually overlap and do not display any significant dispersion. It appears, therefore, that a glass transition did not occur in the RUS samples. Instead, the minima in f^2 seem to mark essentially the same ferroelastic transition as seen in samples with lower Cr contents.

2. Dispersion of acoustic loss

Data for $\tan\delta$ have a narrow peak at the temperature of the minimum in the modulus of 5Cr [Fig. 7(e)]. This is most likely due to a loss mechanism involving mobile interfaces between coexisting phases near the first-order phase transition. Attention has already been drawn to analogous steep increases in Q^{-1} as transition points were approached from above, but the resonance peaks then became too broad to determine whether the same loss mechanism occurred under the relatively low stress, high-frequency conditions of RUS.

The form of variation of $\tan\delta$ below the martensitic transition in the dehydrogenated sample of 5Cr is a plateau of relatively high values which decrease more or less smoothly with falling temperature. Although their magnitudes are much greater than for Q^{-1} , this pattern of acoustic loss is qualitatively similar to the RUS results seen more clearly in Fig. 5. Anelastic loss which occurs due to motion under stress

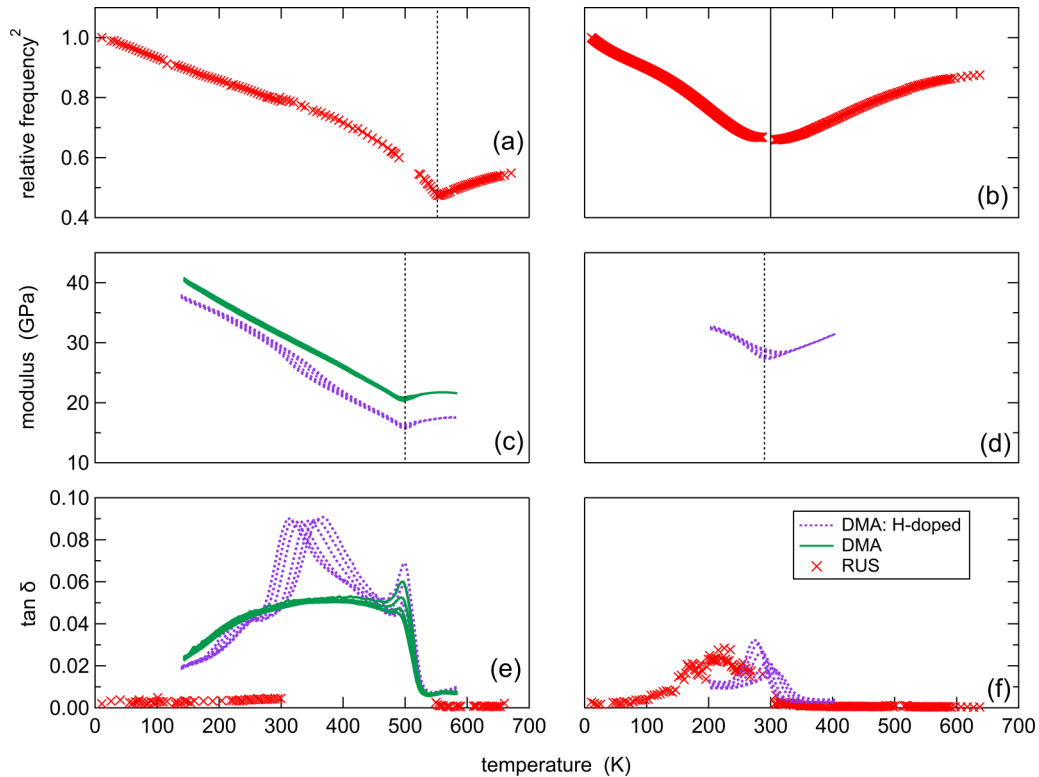


FIG. 7. Elastic modulus and acoustic loss data from RUS and DMA measurements from 5Cr [2] (a),(c),(e), and 10Cr [24] (b),(d),(f) samples. RUS data are shown with red crosses. DMA data for 5Cr are for a hydrogen-doped sample (purple dashed lines) and a hydrogen-free sample (solid green lines). Data for 10Cr are from a sample not treated in any particular way for hydrogen content. Vertical black dotted lines indicate either T_{mfc} (RUS) or T_g (DMA). (a),(b) show the evolution of f^2 with temperature from RUS measurements. (c),(d) include the storage modulus from DMA measurements at frequencies of 0.2–20 Hz. (e),(f) include $\tan\delta$ (DMA), and Q^{-1} (RUS) data divided by $\sqrt{3}$.

of some as yet unspecified component(s) of the ferroelastic microstructure then progressively freezes out with falling temperature.

It is well known for NiTi-based alloys that loss peaks in DMA data arise both from the martensitic transition and from the presence of hydrogen [56]. Consideration of samples with and without hydrogen led to the conclusion that peaks which conformed to Arrhenius behavior with activation energies in the range $\sim 60 - 70 \text{ kJ mole}^{-1}$ were due to the motion of hydrogen in response to dynamical stress. The activation energy for H-related loss in $\text{Ti}_{50}\text{Pd}_{45}\text{Cr}_5$, $\text{Ti}_{50}\text{Pd}_{38}\text{Co}_{12}$, $\text{Ti}_{50}\text{Pd}_{42}\text{Fe}_8$, $\text{Ti}_{50}\text{Pd}_{40}\text{Mn}_{10}$, and $\text{Ti}_{50}\text{Pd}_{42}\text{V}_8$ is in the range $\sim 70 - 90 \text{ kJ mole}^{-1}$, and $1/\omega_0$ is in the range $\sim 10^{-12} - 10^{-14} \text{ s}$ [2,7]. Comparison of hydrogen-doped and hydrogen-free samples by Zhou *et al.* [2] has also led to the conclusion that the frequency-dependent loss peak evident in DMA data from the hydrogen-doped sample [reproduced in Fig. 7(e)], conforms to Arrhenius behavior, with $E_{\text{act}} = 82 \text{ kJ mole}^{-1}$ and $\omega_0 = 10^{13} \text{ s}^{-1}$, and was due to the motion of hydrogen in $\text{Ti}_{50}\text{Pd}_{45}\text{Cr}_5$.

Figure 7(e) shows how loss peaks associated with the martensitic transition are well separated from the Snoek peaks for hydrogen in a sample of 5Cr. It is inevitable, however, that the two loss processes will start to overlap as the martensitic transition temperature reduce with increasing Cr content. DMA data from 9Cr, 10Cr, and 12 Cr show a loss peak near 300 K [3,4,24], and these might be distinguished from the

effects of hydrogen motion if they gave different values of the activation energy from fitting with Arrhenius or Vogel-Fulcher expressions.

C. Anelastic processes in relation to equilibrium phase relationships

Figure 9 shows the results from RUS experiments superimposed on the experimental data and phase boundaries from Fig. 2, which are shown in grey. First, the onset temperature for the development of a tweed texture is not recorded by any acoustic anomalies at temperatures in the range $\sim 500 - 600 \text{ K}$ for 5Cr–12Cr where a change in trend of resistivity with temperature has been seen by Vasseur *et al.* [4]. Second, no anomalies in either f^2 or Q^{-1} have been observed in any of the RUS data at the temperature of the B2-IC phase transition taken to be the temperature at which the electrical resistivity has a minimum [6,8]. This confirms a lack of coupling between the IC order parameter and shear strain, as implied also by the lack of peak splitting in the neutron-diffraction pattern from a sample with $x = 6.5$ at 400 K [27], which is expected to be in the stability field of the incommensurate structure. A lack of coupling of q_{IC} with shear strain e_{ty} would account for the unexpected topology of the phase diagram in comparison with what is expected from classical linear/quadratic order parameter coupling, $\lambda q_{\text{IC}} q_{\text{IC}}^2$, via the combination of $\lambda e_{\text{ty}} q_{\text{IC}}$ and $\lambda q_{\text{ty}} q_{\text{IC}}^2$ (Sec. II above).

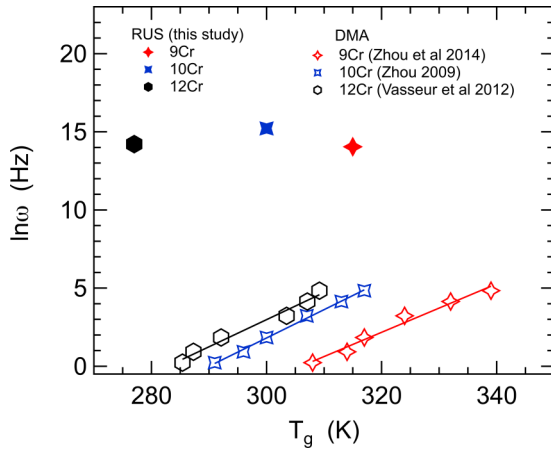


FIG. 8. Comparison of acoustic properties measured for $\text{Ti}_{50}\text{Pd}_{50-x}\text{Cr}_x$ samples using RUS (solid markers) and DMA (hollow markers). DMA data from Zhou *et al.* [3] for 9Cr, Zhou *et al.* [24] for 10Cr, Vasseur *et al.* [4] for 12Cr. ω is the angular frequency of the measurements ($= 2\pi f$). T_g was taken to be the temperature of the minimum in the modulus from DMA or the minimum in f^2 from RUS. Straight lines through the DMA data are guides to the eye. In spite of the large difference in ω between DMA and RUS, the two set of values of T_g overlap.

Without such strain coupling, direct linear/quadratic coupling might be weak and the effective coupling between $q\Gamma$ and q_{1C} would then be biquadratic ($\lambda q_{\Gamma}^2 q_{1C}^2$).

Black circles in Fig. 9 represent RUS values of T_{mfc} and these fall slightly above previous values reported for the martensitic transition temperatures in the range 0Cr–9Cr. The small differences are most likely to be a consequence of not measuring the exact same samples. T_{mfc} is 300 K in 10Cr, which is consistent with changes in synchrotron x-ray-diffraction patterns that show split peaks at 252 K, a shoulder at 300 K, and single peaks at 406 K [4]. Values of T_{mfc} for 10Cr, 11Cr, and 12Cr all fall within or close to the interval

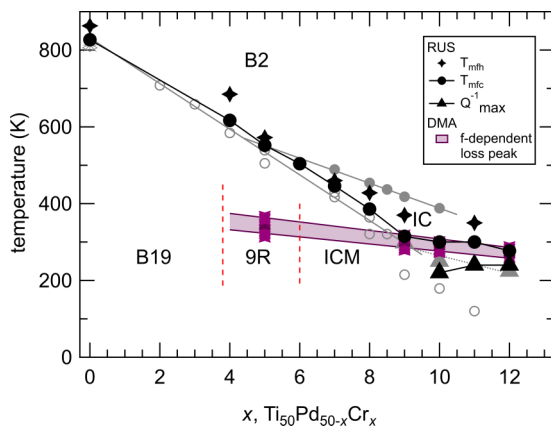


FIG. 9. Phase diagram for the $\text{Ti}_{50}\text{Pd}_{50-x}\text{Cr}_x$ system including RUS results (black markers) and a temperature region of acoustic loss in DMA data (purple shading) which, in the case of 5Cr was attributed to motion of hydrogen [2]. Grey markers indicate the phase diagram shown in Fig. 2.

where the frequency-dependent minimum in storage modulus is present in DMA data.

The temperatures at which maximum values of Q^{-1} were observed in RUS data from samples 9Cr, 10Cr, and 12Cr (filled triangles in Fig. 9) fall below the temperatures at which maxima in $\tan\delta$ were observed in the DMA data. Kinetic analysis indicates that two different loss mechanisms were being sampled, with the loss peak seen by RUS being due to freezing of some component of the ferroelastic microstructure, with $E_{\text{act}} \sim 5 - 10 \text{ kJ mole}^{-1}$, in comparison with higher values which would be attributable to motion of hydrogen. $\tan\delta$ remained high below T_M in the dehydrogenated sample of 5Cr [2], indicating that there were contributions to the loss from the ferroelastic microstructure at low frequencies and relatively high applied stress. Continuing loss processes down to low temperatures are also implied by the trends of Q^{-1} in Fig. 5 but the absolute values are much smaller (Fig. 7).

A purple band in Fig. 9 joins up the temperatures and compositions at which frequency-dependent peaks have been observed in $\tan\delta$. The trend of this zone includes results for 5Cr which were reported to be due to hydrogen [2] and intersects the trend of martensitic transition temperatures at $x \approx 9$. It extrapolates into the temperature/composition interval in which the formation of strain glass has been reported [3,4,24]. The coincidence between transition temperatures from low-frequency DMA data and high-frequency RUS data for 10Cr appears to rule out a strain glass transition mechanism in our samples.

VI. CONCLUSIONS

The phenomenological richness of a martensitic system with doping has been shown to depend on coupling between order parameters relating to different instabilities and their coupling with strain. In particular:

(i) Group theoretical analysis has shown how order parameters with different symmetries combine to give the martensitic and premartensite structures observed in $\text{Ti}_{50}\text{Pd}_{50-x}\text{Cr}_x$. The zone center order parameter with Γ_3^+ symmetry is electronic in origin while the M_5^- and Σ order parameters relate to a soft mode. Linear/quadratic coupling between these is permitted but would not be expected to give rise to the topology of the phase diagram that is actually observed. It is proposed instead that, because coupling of the order parameter for the incommensurate structure with shear strain is weak, the coupling is biquadratic.

(ii) The pattern of softening of the shear modulus with falling temperature ahead of and recovery below the martensitic transition is characteristic of pseudoproper ferroelastic behavior, consistent with the view that the Γ -point instability dominates the strain-relaxation behavior through the bilinear coupling term λe_{Γ} .

(iii) Comparison of data from RUS and DMA show that the temperatures at which a distinct minimum in the shear modulus ($\sim f^2$ from RUS, measured at $\sim 10^5 - 10^6 \text{ Hz}$) and in the Young's modulus (storage modulus from DMA, measured at $\sim 0.1-10 \text{ Hz}$) are closely similar for each sample examined if small changes due to slightly different chemical compositions are taken into account. This applies also for $x = 10$, where a glass transition would have been expected to give

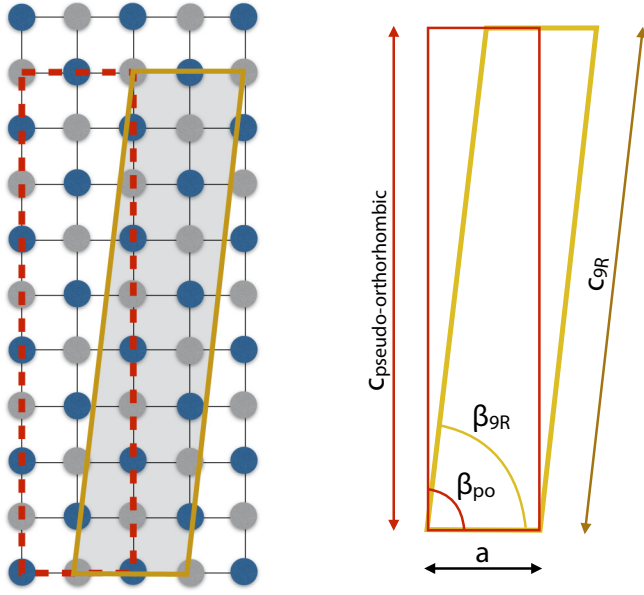


FIG. 10. Relationships between the unit cell of the 9R phase and that of a convenient pseudo-orthorhombic structure used to calculate spontaneous strains. Displacements of individual planes have been ignored for clarity. The pseudo-orthorhombic cell is not a true unit cell, as the atoms at each of the corners are different.

a strong dependence on frequency. The discrepancy conflicts with Vogel-Fulcher dynamics, but the difference in magnitude of stresses involved in the two experimental techniques and in chemical homogeneity of the samples may also be important.

(iv) Temperatures of the peaks in $\tan\delta$ define a trend with composition which crosses the line of martensitic transition temperatures at $x \approx 9$, and are then closely similar to the temperatures at which the minimum in f^2 from RUS measurements for $x = 10, 12$ is observed. Distinguishing between loss peaks due to motion of hydrogen and structural transition peaks at high Cr content should be possible on the basis of different kinetic parameters for samples with systematic variations in H content.

(v) Elevated values of Q^{-1} in RUS data within the stability field of the martensitic structure are attributed to the mobility under stress of some part of the ferroelastic microstructures down to the lowest measuring temperature of ~ 10 K.

ACKNOWLEDGMENTS

This work was supported by the EPSRC/Rolls Royce Strategic Partnership (Grants No. EP/H022309/1 and No. EP/M005607/1). RUS facilities in Cambridge were funded by grants from the Natural Environment Research Council of Great Britain (Grants No. NE/B505738/1 and No. NE/F017081/1).

APPENDIX: STRAIN ANALYSIS

The magnitudes of symmetry-adapted shear strains of the martensitic phases can be estimated using published lattice parameters determined at room temperature, along the lines of formal treatments of spontaneous strains for perovskites such

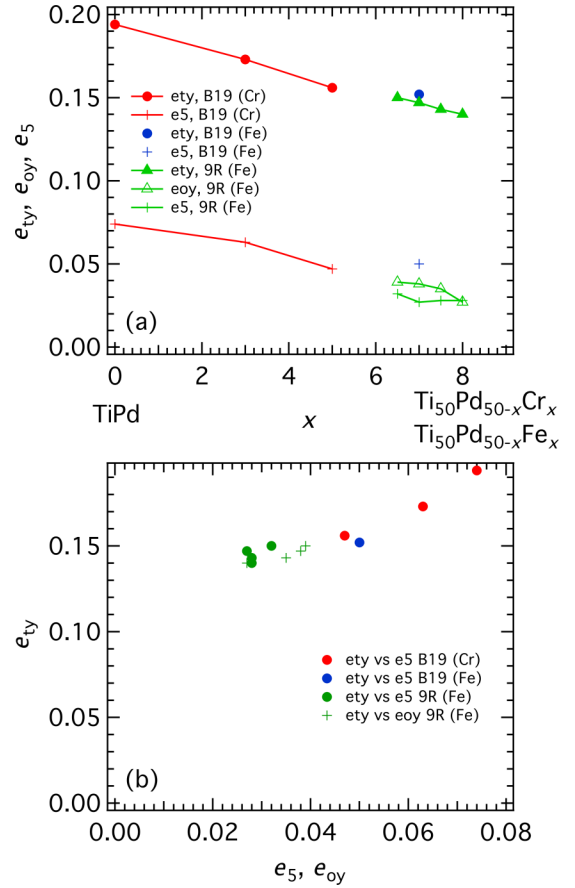


FIG. 11. (a) Symmetry-adapted shear strains for B2-B19 and B2-9R transitions in $\text{Ti}_{50}\text{Pd}_{50-x}\text{Cr}_x$ and $\text{Ti}_{50}\text{Pd}_{50-x}\text{Fe}_x$ as a function of composition at room temperature. (b) Relative changes of symmetry-adapted shear strains for 9R and B19 structures.

as $(\text{Ca}, \text{Sr})\text{TiO}_3$ and SrZrO_3 [59,60]. There are not many data available for $\text{Ti}_{50}\text{Pd}_{50-x}\text{Cr}_x$ so these have been supplemented with data for $\text{Ti}_{50}\text{Pd}_{50-x}\text{Fe}_x$ which displays closely similar behavior. Pseudocubic lattice parameters (with subscript pc) are related to the lattice parameters of the B19 structure according to

$$a_{\text{pc}} = \frac{a_{\text{B19}}}{\sqrt{2}}, \quad b_{\text{pc}} = b_{\text{B19}}, \quad c_{\text{pc}} = \frac{c_{\text{B19}}}{\sqrt{2}}. \quad (\text{A1})$$

Using reference axes x_1, x_2, x_3 parallel to crystallographic x, y, z axes of the parent cubic structure in space group $Pm\bar{3}m$, the six components of the spontaneous strain tensor are given by (following Refs. [59,60])

$$e_3 + e_1 = \frac{\frac{c_{\text{B19}}}{\sqrt{2}} - a_0}{a_0} + \frac{\frac{a_{\text{B19}}}{\sqrt{2}} - a_0}{a_0}, \quad e_2 = \frac{b_{\text{B19}} - a_0}{a_0},$$

$$e_5 = \frac{\frac{c_{\text{B19}}}{\sqrt{2}} - a_0}{a_0} - \frac{\frac{a_{\text{B19}}}{\sqrt{2}} - a_0}{a_0}, \quad e_4 = e_6 = 0. \quad (\text{A2})$$

The lattice parameter of the B2 phase extrapolated into the B19 stability field a_0 is approximated for a cubic \rightarrow orthorhombic transition by taking the arithmetic mean of the

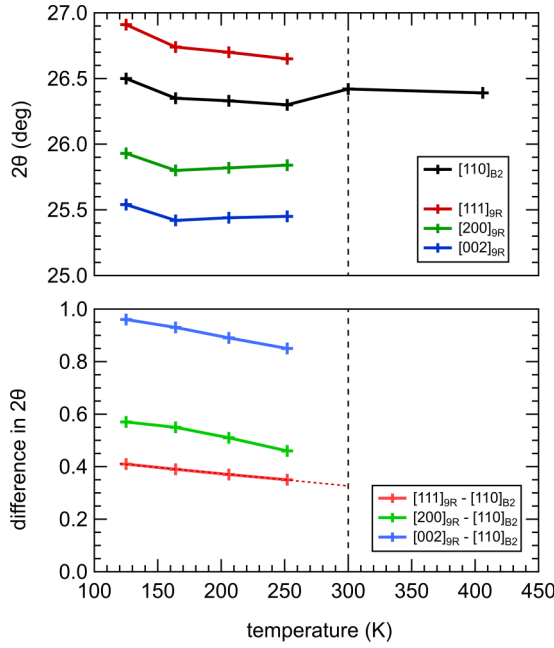


FIG. 12. Peak positions and peak splitting in x-ray-diffraction patterns for 10Cr, as extracted from Fig. 6 of Vasseur *et al.* [4]. Top: peak positions. Bottom: difference in angle between the 9R and B2 peaks.

pseudocubic lattice parameters:

$$a_o = \frac{a_{pc} + b_{pc} + c_{pc}}{3}. \quad (\text{A3})$$

The symmetry-adapted orthorhombic strain $e_{oy}(= e_3 - e_1)$ is zero and the tetragonal strain, e_{ty} , is given by

$$e_{ty} = \frac{1}{\sqrt{3}}(2e_2 - e_3 - e_1). \quad (\text{A4})$$

The unique crystallographic axis for the structures with a Γ_3^+ order parameter has been taken as being parallel to the crystallographic y axis of the parent structure in $Pm\bar{3}m$.

Settings of the 9R structure for strain calculations are awkward to visualize, but the relationships chosen here are shown schematically in Fig. 10. Solid yellow lines in the sketch on the left-hand side show a nine-layer repeat for the monoclinic 9R structure. Dashed red lines show a convenient pseudo-orthorhombic cell, though this is not a true unit cell because atoms at the corners are different. The sketch on the right-hand side shows the relationship between the a , c , and β of the two cells. Subscripts po and 9R refer to the pseudo-orthorhombic cell and 9R cell parameters, respectively.

The pseudocubic parameters for the pseudo-orthorhombic form of the 9R phase at room temperature are

$$a_{pc} = \frac{a_{9R}}{\sqrt{2}}, \quad b_{pc} = b_{9R}, \quad c_{pc} = \frac{c_{po}}{4.5 \times \sqrt{2}}, \quad (\text{A5})$$

TABLE III. Lattice parameters from the literature and symmetry-adapted strains calculated from them for the B19 phase of $\text{Ti}_{50}\text{Pd}_{50-x}\text{Cr}_x$ alloys at room temperature.

Composition	Lattice parameters (nm)			Strains		Ref.
	a	b	c	e_{ty}	e_5	
TiPd	0.456	0.281	0.489	0.194	0.074	[62]
3% Cr	0.453	0.283	0.481	0.173	0.063	[9]
5% Cr	0.454	0.286	0.475	0.156	0.047	[9]
7% Fe	0.452	0.286	0.474	0.152	0.050	[9]

and the six strain components, with the same reference system as before, are

$$\begin{aligned}
 e_3 + e_1 &= \frac{\left(\frac{c_{po} \sin \beta_o}{4.5 \times \sqrt{2}}\right) - a_o}{a_o} + \frac{\frac{a_{9R}}{\sqrt{2}} - a_o}{a_o} \\
 &\approx \frac{\frac{c_{po}}{4.5 \times \sqrt{2}} - a_o}{a_o} + \frac{\frac{a_{9R}}{\sqrt{2}} - a_o}{a_o}, \\
 e_2 &= \frac{b_{9R} - a_o}{a_o}, \quad e_4 = e_6 = 0, \\
 e_5 &= \frac{\left(\frac{c_{po} \sin \beta_o}{4.5 \times \sqrt{2}}\right) - a_o}{a_o} + \frac{\frac{a_{9R}}{\sqrt{2}} - a_o}{a_o} \\
 &\approx \frac{\frac{c_{po}}{4.5 \times \sqrt{2}} - a_o}{a_o} + \frac{\frac{a_{9R}}{\sqrt{2}} - a_o}{a_o}, \\
 e_{oy} &= \frac{c_{po}}{4.5 \times \sqrt{2} a_o} \cos \beta_{po} \approx \cos \beta_{po}. \quad (\text{A6})
 \end{aligned}$$

The symmetry-adapted tetragonal strain is again given by Eq. (A4). Note that the form of the equations for e_5 and e_{oy} incorporate rotation of the pseudo-orthorhombic cell through 45° with respect to the reference axes. The equation for e_{oy} then follows from Eq. (35) of Carpenter *et al.* [61].

Lattice parameters for the B19 and 9R structures at room temperature and symmetry-adapted shear strains calculated from them are given in Tables III and IV, respectively. The angle β_{po} was calculated to be slightly larger than 90° , showing that the 9R unit cell of $\text{Ti}_{50}\text{Pd}_{50-x}\text{Fe}_x$ is truly monoclinic. Values of e_{ty} are $\sim 15\text{--}20\%$, which is typical of martensites but very substantially greater than the ferroelastic shear strain which accompanies ferroelastic transitions in functional oxides ($\sim 2\text{--}5\%$). Values of e_5 vary between ~ 3 and 7% , while e_{oy} for the 9R structure is $\sim 3\text{--}4\%$. As shown in Fig. 11(a), the trend for all three values is of a slight decrease with increasing concentration of dopant. If the driving order parameter for the B2-B19 transition had the symmetry of irrep M_5^- alone, the expected relationship with the symmetry-breaking strains would be $e_{ty} \propto e_5 \propto q_M^2$. This would give data for e_{ty} and e_5 lying along a straight line that passes through zero. The fact that they do not [Fig. 11(b)] is consistent with the view that the transition is driven also by the Γ_3^+ order parameter.

There appears to be no equivalent data in the literature which would allow determination of the values of these shear strains as a function of temperature, but peak splitting in diffraction patterns given by Vasseur *et al.* [4] can be used

TABLE IV. Lattice parameters from the literature and symmetry-adapted strains calculated from them for the 9R phase of $\text{Ti}_{50}\text{Pd}_{50-x}\text{Fe}_x$.

Comp.	Lattice parameters (nm, deg)						Strains						Ref.
	a_{9R}	b_{9R}	c_{9R}	β_{9R}	c_{po}	β_{9po}	a_{pc}	b_{pc}	c_{pc}	e_{ty}	e_5	e_{oy}	
6.5Fe	0.469	0.286	2.053	85.6	2.048	92.2	0.332	0.286	0.322	0.150	0.032	0.039	[6]
7Fe	0.467	0.286	2.053	85.6	2.048	92.1	0.330	0.286	0.322	0.147	0.027	0.038	[6]
7.5Fe	0.467	0.287	2.053	85.4	2.047	91.9	0.330	0.287	0.322	0.143	0.028	0.035	[6]
8Fe	0.467	0.288	2.054	85.0	2.047	91.5	0.330	0.288	0.322	0.140	0.028	0.027	[6]

as a proxy for the distortion from cubic lattice geometry for 10Cr. The positions of peaks from the 9R phase extracted from Fig. 6 of Vasseur *et al.* [4] and their differences from the peak corresponding to the B2 structure in degrees 2θ are shown in Fig. 12. The peak splitting decreases with increasing temperature but, when extrapolated towards the phase-transition

temperature (marked with the grey dashed line), the difference does not reach zero. This is consistent with the view that the transition at ~ 300 K is first order in character. By way of contrast, the 12Cr sample appears to not show peak splitting at any of the temperatures at which diffraction patterns were collected (125–406 K) [4].

- [1] Y. Zhou, D. Xue, X. Ding, K. Otsuka, J. Sun, and X. Ren, *Phys. Status Solidi B* **251**, 2027 (2014).
- [2] Y. Zhou, G. Fan, D. Xue, X. Ding, K. Otsuka, J. Sun, and X. Ren, *Scr. Mater.* **61**, 805 (2009).
- [3] Y. Zhou, D. Xue, Y. Tian, X. Ding, S. Guo, K. Otsuka, J. Sun, and X. Ren, *Phys. Rev. Lett.* **112**, 025701 (2014).
- [4] R. Vasseur, D. Xue, Y. Zhou, W. Ettoumi, X. Ding, X. Ren, and T. Lookman, *Phys. Rev. B* **86**, 184103 (2012).
- [5] H. C. Donkersloot and J. H. N. Van Vucht, *J. Less Common Met.* **20**, 83 (1970).
- [6] K. Enami and Y. Nakagawa, in *Proceedings of the International Conference on Martensitic Transformations*, ICOMAT Vol. 92 (Monterey Institute Advanced Studies, Monterey, 1992), p. 521.
- [7] D. Xue, Y. Zhou, X. Ding, K. Otsuka, T. Lookman, J. Sun, and X. Ren, *Mater. Sci. Eng. A* **632**, 110 (2015).
- [8] K. Enami, K. Hori, and J. Takahashi, *ISIJ Int.* **29**, 430 (1989).
- [9] O. Yoshinari and D. Itoh, *Mater. Sci. Forum* **561-565**, 2353 (2007).
- [10] Y. Murakami, S. Kidu, and D. Shindo, *J. Phys. IV France* **112**, 1031 (2003).
- [11] M. Todai, T. Fukuda, and T. Kakeshita, *Mater. Lett.* **108**, 293 (2013).
- [12] Y. Yamabe-Mitarai, A. Wadwood, R. Arockiakumar, T. Hara, M. Takahashi, S. Takahashi, and H. Hosoda, *Mater. Sci. Forum* **783-786**, 2541 (2014).
- [13] Y. Xu, K. Otsuka, E. Furubayashi, T. Ueki, and K. Mitose, *Mater. Lett.* **30**, 189 (1997).
- [14] W. Cai, K. Otsuka, and M. Asai, *Mater. Trans. JIM*, **40**, 895 (1999).
- [15] P. G. Lindquist and C. M. Wayman, in *Engineering Aspects of Shape Memory Alloys*, edited by T. Duerig, K. Melton, D. Stöckel, and C. Wayman (Butterworth-Heinemann, London, 1990), p. 58.
- [16] D. Goldberg, Y. Xu, Y. Murakami, K. Otsuka, T. Ueki, and H. Horikawa, *Mater. Lett.* **22**, 241 (1995).
- [17] P. K. Kumar and D. C. Lagoudas, *Acta Mater.* **58**, 1618 (2010).
- [18] D. Goldberg, Y. Xu, Y. Murakami, S. Morito, K. Otsuka, T. Ueki, and H. Horikawa, *Scr. Met.* **30**, 1349 (1994).
- [19] S. Shimizu, Y. Xu, E. Okunishi, S. Tanaka, K. Otsuka, and K. Mitose, *Mater. Lett.* **34**, 23 (1998).
- [20] J. Frenzel, A. Wiczorek, I. Opahle, B. Maab, R. Drautz, and G. Eggeler, *Acta Mater.* **90**, 213 (2015).
- [21] M. Todai, T. Fukuda, and T. Kakeshita, *J. Alloys Compd.* **615**, 1047 (2014).
- [22] K. Otsuka, K. Oda, Y. Ueno, M. Piao, T. Ueki, and H. Horikawa, *Scr. Met.* **29**, 1355 (1993).
- [23] M. Kawakita, M. Takahashi, S. Takahashi, and Y. Yamabe-Mitarai, *Mater. Lett.* **89**, 336 (2012).
- [24] Y. Zhou, D. Xue, X. Ding, K. Otsuka, J. Sun, and X. Ren, *Appl. Phys. Lett.* **95**, 151906 (2009).
- [25] A. J. Schwartz, S. Paciornik, R. Kilaas, and L. E. Tanner, *J. Microsc.* **180**, 51 (1995).
- [26] N. Matveeva, Yu. Kovneristyi, A. Savinov, V. Sivokha, and V. Khachin, *J. Phys. Colloq.* **43**, C4-249 (1982).
- [27] S. M. Shapiro, G. Xu, B. L. Winn, D. L. Schlagel, T. Lograsso, and R. Erwin, *Phys. Rev. B* **76**, 054305 (2007).
- [28] C. J. Howard, Z. Zhang, M. A. Carpenter, and K. S. Knight, *Phys. Rev. B* **76**, 054108 (2007).
- [29] D. Viehland, M. Wuttig, and L. E. Cross, *Ferroelectrics* **120**, 71 (1991).
- [30] A. Levstik, Z. Kutnjak, D. Filipic, and R. Pirc, *Phys. Rev. B* **57**, 11204 (1998).
- [31] A. E. Glazounov and A. K. Tagantsev, *Appl. Phys. Lett.* **73**, 856 (1998).
- [32] A. A. Bokov and Z.-G. Ye, *Phys. Rev. B* **74**, 132102 (2006).
- [33] D. Xue, R. Yuan, Y. Zhou, D. Xue, T. Lookman, G. Zhang, X. Ding, and J. Sun, *Sci. Rep.* **6**, 28244 (2016).
- [34] M. A. Carpenter and Z. Zhang, *Geophys. J. Int.* **186**, 279 (2011).
- [35] M. A. Carpenter, *J. Phys.: Condens. Matter* **27**, 263201 (2015).
- [36] J. N. Walsh, P. A. Taylor, A. Buckley, T. W. Darling, J. Schreuer, and M. A. Carpenter, *Phys. Earth Planet. Int.* **167**, 110 (2008).
- [37] K. Otsuka, T. Ohba, M. Tokonami, and C. Wayman, *Scr. Met.* **29**, 1359 (1993).
- [38] H. T. Stokes, D. M. Hatch, and B. J. Campbell, ISOTROPY, <http://stokes.byu.edu/isotropy.html>.

- [39] M. A. Carpenter and C. J. Howard, *Acta Crystallogr., Sect. B* **74**, 560 (2018).
- [40] K. Otsuka and X. Ren, *Prog. Mater. Sci.* **50**, 511 (2005).
- [41] G. R. Barsch, *Mater. Sci. Forum* **327–328**, 367 (2000).
- [42] M. A. Carpenter and E. K. H. Salje, *Eur. J. Mineral.* **10**, 693 (1998).
- [43] E. K. H. Salje and M. A. Carpenter, *J. Phys.: Condens. Matter* **23**, 462202 (2011).
- [44] A. Schwartz, M. Sluiter, B. Harmon, and L. Tanner, in *Proceedings of an International Conference on Solid-solid Phase Transformations* (The Minerals, Metals and Materials Society, Pittsburg, 1994), p. 911.
- [45] A. J. Schwartz and L. E. Tanner, *Scr. Met.* **32**, 675 (1995).
- [46] R. E. A. McKnight, M. A. Carpenter, T. W. Darling, A. Buckley, and P. A. Taylor, *Am. Mineral.* **92**, 1665 (2007).
- [47] R. E. A. McKnight, T. Moxon, A. Buckley, P. A. Taylor, and M. A. Carpenter, *J. Phys.: Condens. Matter* **20**, 075229 (2008).
- [48] A. Migliori and J. L. Sarrao, *Resonant Ultrasound Spectroscopy: Applications to Physics, Materials Measurements and Nondestructive Evaluation* (Wiley, New York, 1997).
- [49] R. J. Harrison and S. A. T. Redfern, *Phys. Earth Planet. Inter.* **134**, 253 (2002).
- [50] R. J. Harrison, S. A. T. Redfern, and E. K. H. Salje, *Phys. Rev. B* **69**, 144101 (2004).
- [51] M. A. Carpenter, A. Buckley, P. A. Taylor, and T. W. Darling, *J. Phys.: Condens. Matter* **22**, 035405 (2010).
- [52] E. K. H. Salje, H. Zhang, H. Idrissi, D. Schryvers, M. A. Carpenter, X. Moya, and A. Planes, *Phys. Rev. B* **80**, 134114 (2009).
- [53] R. Schaller, G. Fantozzi, and G. Gremaud, *Mechanical Spectroscopy Q-1 2001: With Applications to Materials Science* (Trans Tech Publications, Clausthal, Germany, 2001).
- [54] I. S. Golovin, S. Divinski, J. Cízek, I. Procházka, and F. Stein, *Acta Mater.* **53**, 2581 (2005).
- [55] A. S. Nowick and B. S. Berry, *Anelastic Relaxation in Crystalline Solids* (Academic, New York, 1972).
- [56] G. Mazzolai, *AIP Adv.* **1**, 040701 (2011).
- [57] T. Lee, R. S. Lakes, and A. Lal, *Rev. Sci. Instrum.* **71**, 2855 (2000).
- [58] R. S. Lakes, *Rev. Sci. Instrum.* **75**, 797 (2004).
- [59] M. A. Carpenter, A. I. Becerro, and F. Seifert, *Am. Mineral.* **86**, 348 (2001).
- [60] R. E. A. McKnight, C. J. Howard, and M. A. Carpenter, *J. Phys.: Condens. Matter* **21**, 015901 (2009).
- [61] M. A. Carpenter, E. K. H. Salje, and A. Graeme-Barber, *Eur. J. Mineral.* **10**, 619 (1998).
- [62] A. E. Dwight, R. A. Conner, and J. W. Downey, *Acta Crystallogr.* **18**, 837 (1965).